Dalton Transactions

Accepted Manuscript

ROYAL SOCIETY OF CHEMISTRY

www.rsc.org/dalton

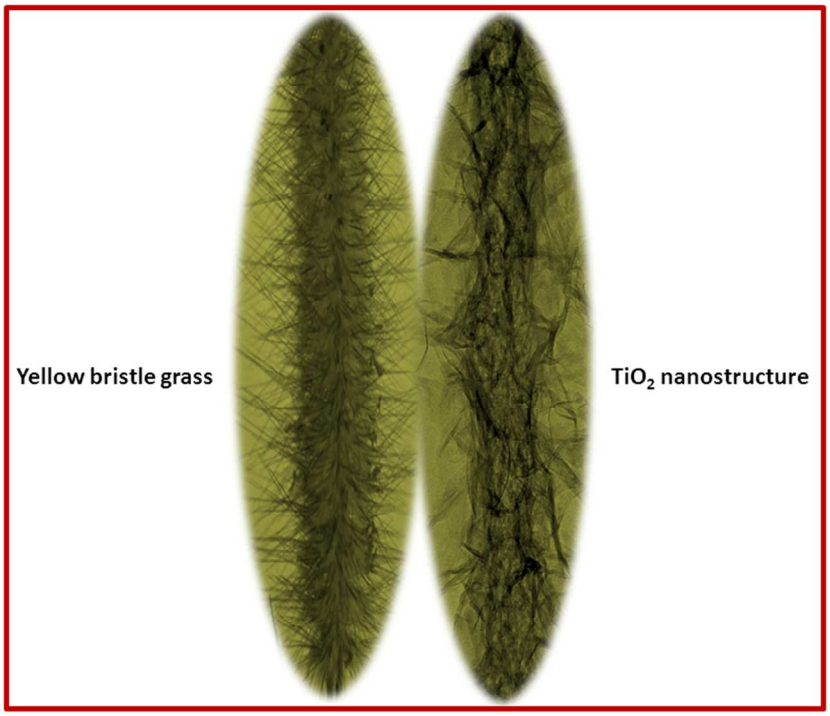

254x190mm (96 x 96 DPI)

Journal Name

RSCPublishing

ARTICLE

TiO_2 nanofibers resembling 'yellow bristle grass' in morphology by a soft chemical transformation†

Cite this: DOI: 10.1039/x0xx00000x

Received 00th January 2012,
Accepted 00th January 2012

DOI: 10.1039/x0xx00000x

www.rsc.org/

Sandeep Nandan, T. G. Deepak, Shantikumar V Nair and A. Sreekumaran Nair*

We synthesized a uniquely shaped one-dimensional (1-D) TiO_2 nanostructure having the morphology of yellow bristle grass with high surface area by titanate route under soft reaction conditions. The electrospun TiO_2-SiO_2 composite nanofibers upon treatment with concentrated NaOH at 80 ^{0}C under ambient pressure for 24 h resulted in sodium titanate ($Na_2Ti_3O_7$) nanostructures. The $Na_2Ti_3O_7$ nanostructures have an overall 1-D fibrous morphology but the highly porous fiber surfaces were decorated with layered thorn-like features (a morphology resembling that of *yellow bristle grass*) resulting in high surface area (113 m^2/g) and porosity. The $Na_2Ti_3O_7$ nanostructures were converted into TiO_2 nanostructures of the same morphology by acidification (0.1 N HCl) followed by low temperature sintering (110 ^{0}C) processes. Dye-sensitized solar cells (DSCs) constructed out of the material (cells of area 0.20 cm^2 and thickness of 12 μm) showed a power conversion efficiency (η) of 8.02 % in comparison to commercial P-25 TiO_2 (η = 6.1 %).

Introduction

TiO_2 is a versatile material having applications in various fields such as renewable energy harvesting (especially dye- and perovskite-sensitized solar cells (DSCs/PSSCs)),[1-5] energy storage (Li-ion batteries, supercapacitors, etc.),[6-8] photocatalysis (water splitting),[9-12] environmental remediation,[13-15] photonic crystals,[16] self-cleaning coatings,[17] etc. For most of the applications mentioned above, TiO_2 with a high surface area (and porosity) is preferred. There are two ways to increase the surface area of TiO_2 in a TiO_2 nanostructure: one is to reduce the size of the particles in the nanoarchitecture and the other is to increase its porosity. One-dimensional TiO_2 nanostructures such as nanofibers, nanowires and nanotubes find renewed interests for the above mentioned applications because of guided/semi-guided electron transport, scattering of solar photons corresponding to the red part of the solar spectrum, etc.[18-20] However, the TiO_2 nanofibers inherently have a low internal surface area which is particularly true for the electrospun TiO_2 nanofibers (~ 44 m^2/g).[21-22] The fabrication of electrospun TiO_2 nanofibers involves a high temperature sintering at 450 ^{0}C and during the process the sizes of the particles in the nanofiber architecture increase which results in loss of surface area for the fibers.[21-22] Further, the nanofibers are formed out of fusion of particles which results in loss of internal surface area for the former.[21-22] Thus increasing the surface area of the electrospun TiO_2 nanofibers through size reduction of constituting particles in the fibers is not a feasible approach. The second approach of roughening the surface through chemical means is a facile one. Previously we have shown that etching ZnO from rice-shaped TiO_2-ZnO composite leads to coral reef-shaped TiO_2 nanostructures with good photovoltaic and photocatalytic properties.[23] In the present paper we show that a soft etching of SiO_2 from electrospun TiO_2-SiO_2 composite nanofibers with the *in-situ* chemical transformation of the TiO_2 using the sodium titanate process produces a fascinating morphology for the TiO_2, which is *yellow bristle grass-like*. The TiO_2 had a surface area of 113 m^2/g which when tested for a DSC showed a conversion efficiency of 8.02% for a cell of area 0.2 cm^2 and thickness ~ 12 μm. It must be noted that the present morphology appears only under soft reaction conditions[24] (treatment with

concentrated NaOH at 80 ^{0}C, ambient pressure) and under rigorous conditions (such as the hydrothermal reaction with concentrated NaOH, 180 ^{0}C in a typical steel-lined autoclave) the product was always 2-D (such as leaf) and 3-D (such as flowers) morphologies of TiO_2.[24-26]

Experimental

a) Chemicals needed

PVP (polyvinylpyrrolidone, Mw=1.3×10^6, mp. 300 ^{0}C, Aldrich, Steinhseim, Germany), methanol (Aldrich, Steinhseim, Germany), acetic acid (LR, Nice Chemicals, India), titanium (IV) isopropoxide (TiP, 97%, Aldrich, Germany), tetraethoxysilane (TES, 98% GC grade, Alfa Aesar, UK), sodium hydroxide pellets (A.R, Nice Chemicals, India), hydrochloric acid (ACS, ISO Reag. Merk KGaA, Germany), and N719 dye (Solaronix SA) were used as received. Fluorine-doped tin oxide plates (FTO, sheet resistance of 6-8 Ω/□) were fabricated in-house by spray-pyrolysis deposition method. The precursors of the FTO solution were made of dibutyltin diacetate (DBTDA) in 2-propanol (0.2 M) and ammonium fluoride (NH4F) in water (9 M).

b) Fabrication of TiO_2-SiO_2 Composite nanofibers

The TiO_2-SiO_2 composite nanofibers (NFs) were fabricated by electrospinning technique.[24a] Typically; about 1 g of PVP was dissolved in 14 mL of methanol followed by the addition of 4 mL of acetic acid, 1.75 mL of TiP and 0.25 mL of TES, respectively. The polymeric solution containing the precursors was subjected to continuous magnetic stirring for 5 h at room temperature to get sufficient viscosity and homogeneity for electrospinning. Electrospinning was done using a humidity-controlled electrospinning set-up (IME Technologies, The Netherlands) under the optimized conditions of 30 kV and with a flow rate of 1 mL h^{-1}. The humidity level inside the electrospinning chamber was maintained at ~ 50%. The as-spun composite fibers were collected on an Al foil which is wrapped to a static metallic collector. The distance between the needle tip and the collector was kept at 10 cm. The as-pun fibers were collected in the form of white sheet on the Al foil and which was peeled-off and sintered at 450 ^{0}C for 3 h for removing the polymer and crystallizing the TiO_2-SiO_2 composite. The as-spun composite (TiO_2-SiO_2-PVP) was characterized by scanning electron microscopy (SEM) and the sintered (TiO_2-SiO_2) nanofibers were analysed by spectroscopy and microscopy, respectively, as detailed below in the manuscript.

b) Synthesis of titanate fibers from the TiO_2-SiO_2 composite nanofibers

About 500 mg of the TiO_2-SiO_2 composite nanofibers was suspended in a 100 mL glass bottle containing 5 M NaOH solution without stirring. The glass bottle was subsequently kept in a hot air oven at 80 ^{0}C for 24 h. The TiO_2-SiO_2 composite has turned into a fluffy white precipitate of $Na_2Ti_3O_7$ (sodium titanate) which was washed many times with deionized water and finally with methanol and dried in an oven at 60 ^{0}C. The titanate thus obtained was characterized with spectroscopic, microscopic and surface area measurements. The purpose of fabricating a composite architecture (TiO_2-SiO_2 composite fiber) was that SiO_2 is an acidic metal oxide and can be easily etched using a base like NaOH during the titanate process. Etching of SiO_2 from TiO_2-SiO_2 composite fibers would give higher surface area for the sodium titanate.

c) Synthesis of titanate-derived yellow bristle grass-like TiO_2 from the titanate fibers

The fluffy white titanate was suspended in dil. HCl (0.1 M HCl) at room temperature for 24 h. The resulted protonated titanate ($H_2Ti_3O_7$) was then washed several times with deionized water and finally with methanol and dried in an oven at 110 ^{0}C for 24 h. During the heat treatment, the $H_2Ti_3O_7$ gets converted into TiO_2 (the titanate-derived TiO_2) with thorn-like features on the nanofiber backbone. The TiO_2 was characterized by spectroscopy, microscopy and BET surface area analysis.

d) Fabrication of dye-sensitized solar cells (DSCs)

Dye-sensitized solar cells (DSCs) were fabricated with the thorn-like TiO_2 fibers by doctor-blading technique. The polymer used for making the TiO_2 paste was polyester which was prepared by the polycondensation of citric acid and ethylene glycol as reported before.[25a] About 100 mg of the TiO_2 fibers was mixed with 100 μL of polyester and sonicated for 10 h to get a unique paste for doctor-blading. The TiO_2 paste was doctor-bladed onto the Fluorine-doped tin oxide (FTO) plates which had a prior thin TiO_2 coating (of ~ 100 nm thickness) by spray pyrolysis deposition method.[25b] The doctor-bladed films had a thickness of around 15 μm. We also made similar films from the commercially available P-25 for a comparison. The doctor-bladed FTO plates were sintered at 450 ^{0}C for 1 h during which the polymer got degraded and removed resulting in an optimum electrode thickness of ~11 to 12 μm for the TiO_2. The porous TiO_2 films were subsequently immersed in aq. $TiCl_4$ solution (30 mM, 70 ^{0}C) for 30 min and again sintered at 450 ^{0}C for 1 h. The sintered electrodes were socked in 0.5 mM N719 dye solution in 1:1 acetonitrile-tert-butanol mixture for 24 h at room temperature and washed with absolute methanol for removing the loosely bound dyes. The electrodes having an active area of 0.25 cm^2 were placed against platinum (Pt sputter-coated) counter-electrodes in the presence of a parafilm spacer and I_3^-/I^- electrolyte for DSC fabrication.

Characterization

The initial TiO_2-SiO_2 composite, the sodium titanate and the final titanate-derived TiO_2 were characterized by spectroscopy and microscopy. The scanning electron microscopy (SEM) was performed using a JSM 6490 LA (JEOL-Tokyo, Japan) machine at an operating voltage of 15 kV. The samples spread on glass were coated with a thin film of gold before SEM measurements. High-resolution transmission electron microscopy (HR-TEM) was done with the JEOL 3010 machine

at an operating voltage of 300 kV. A suspension of the samples was made in methanol under sonication and a drop of the solution was caste on a carbon-coated TEM grid which was subsequently dried in ambience and in vacuum, respectively. The surface area of the materials was analyzed by the BET (Brunauer-Emmett-Teller) N_2 adsorption method using a BET Analyzer ((Model No. Nova 1200 series from Quantachrome (USA)). Pore size distribution and average pore volume were estimated from the BET measurement using the manufacturer's software. The powder XRD measurements were performed on each sample by an X'pert pro PAN Analytical operated at 30 mA current and with a voltage 40 kV. X-ray photo electron spectroscopy (XPS) was performed with a machine from Kratos Analytical, UK. The materials were characterized by Raman spectroscopy as well using a Witec confocal Raman-300 AR instrument (with an excitation laser of 488 nm and power of 0.6 mW). Current-voltage (*I–V*) characteristics of the DSCs were probed by a solar simulator under AM 1.5G condition (Newport Oriel class A-Solar simulator, USA). The wavelength-dependent incident photon-to-current conversion efficiency (IPCE) was measured using an Oriel Newport (QE-PV-SI/QE) IPCE Measurement kit, USA. The electron lifetime and recombination resistance of the DSCs were analyzed using electrochemical impedance spectroscopy (EIS) in dark under an applied bias voltage of 0.69 V by using an Autolab (Metrohm, Newport model, The Netherlands).

Results and discussion

a) Characterization of TiO_2-SiO_2 composite nanofibers, the intermediate sodium titanate and the final titanate-derived TiO_2

Fig. 1 shows the SEM images of as-spun TiO_2-SiO_2-PVP composite nanofibers and the sintered TiO_2-SiO_2 nanofibers. Fibers were smooth and nearly continuous with an average diameter ranging from 200-250 nm (Fig. 1A and 1B). Upon sintering at 450 ^{0}C for 3 h, the polymer degradation (reduction in the fiber diameter) and crystallization of the metal oxide grains occurred which results in continuous composite fibers of TiO_2-SiO_2 of 100-150 nm diameter range. Fig. 1(C and D) gives the details of TiO_2–SiO_2 composites after sintering. Fig. 2A shows the large area TEM image of TiO_2-SiO_2 nanofibers. Fig. 2B and 2C shows the magnified image of a single nanofiber. Fig. 2D shows the high-resolution TEM image which indicates the amorphous nature of the SiO_2 in the TiO_2-SiO_2 composite.[26-28] The lattice spacing of 0.35 nm corresponds to the (101) lattice and this indicates the anatase phase of the TiO_2 in the TiO_2-SiO_2 composites. Lattice spacing corresponding to the SiO_2 was absent in the lattice-resolved image implying that SiO_2 is in amorphous phase. The TiO_2-SiO_2 nanofibers were further analyzed by powder XRD, Raman spectroscopy, BET surface area and XPS measurements. The peaks in XRD spectrum (Fig. 3A) further confirm the anatase phase of the TiO_2 and the amorphous nature of SiO_2 in the composite (*i.e.* the absence of peaks corresponding to the SiO_2).[28] From the Raman spectra (Fig. 3B) the bands at 152 cm^{-1}, 430 cm^{-1} and 517 cm^{-1} show anatase phase of the TiO_2 while the other peaks (612 cm^{-1} and 253 cm^{-1}) indicate the amorphous SiO_2.[29] The BET surface area of the TiO_2-SiO_2 composites was 53 m^2/g. Fig. 4a shows the XPS wide spectrum of the TiO_2-SiO_2 composite and the high-resolution spectra of the elements are shown in Fig. 4b-d. The binding energies of Ti 2p3/2 and Ti 2p1/2 were centered at 458.46 eV and 464.16 eV, respectively, which corresponds to a spin-orbit coupling of 5.7 eV.[28,30] The O 1s peak shown in the Fig. 4c was de-convoluted into two peaks at 529.7 eV and 531 eV, respectively, corresponding to the presence of Ti-O-Ti and Si-O-Si bonds.[31]

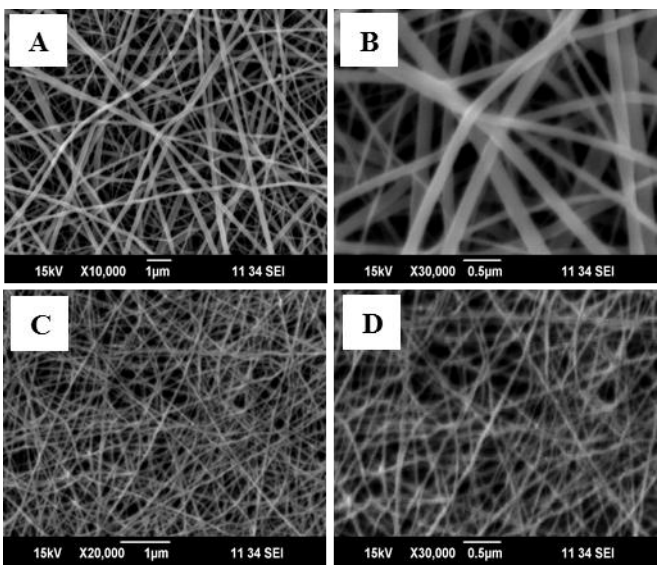

Fig. 1. SEM images of (A and B) as-spun TiO_2-SiO_2-PVP composite nanofibers and (C and D) TiO_2-SiO_2 composite nanofibers after sintering at 450 ^{0}C.

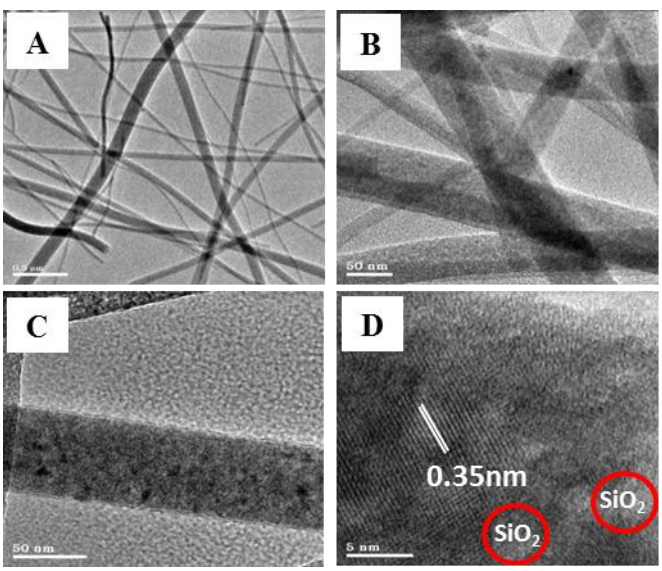

Fig. 2. TEM analysis (A) large area TEM image of TiO_2-SiO_2 nanofibers, (B) and (C) respectively show magnified images of a few nanofibers and a single nanofiber and (D) shows a lattice-resolved TEM image of a single TiO_2-SiO_2 nanofiber where red circled area indicates the regions of amorphous SiO_2 and the lattice spacing of 0.35 nm shows anatase TiO_2.

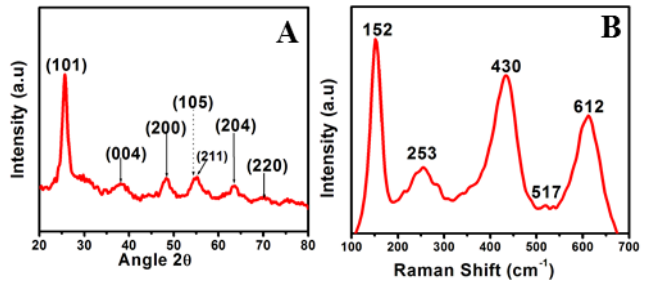

Fig. 3. XRD (Fig. 3A) and RAMAN (Fig. 3B) analysis of TiO_2-SiO_2 composites.

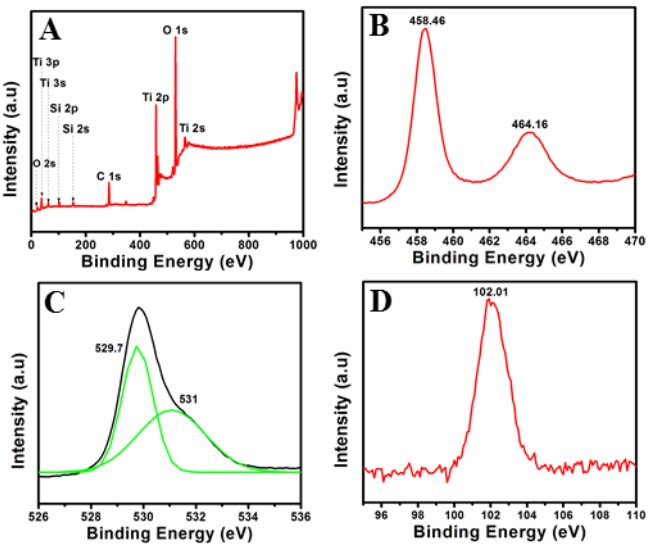

Fig. 4. XPS wide spectrum (Fig. **A**) of TiO_2-SiO_2 composites and the high-resolution spectra of Ti (**B**), O (**C**) and Si (**D**), respectively.

This confirms the SiO_2 incorporation into the TiO_2 matrix through Ti-O-Si bonds.[31] The peak for Si was centered at a binding energy of 102.01 eV as evident from Fig. 4d.

On alkali treatment (*i.e.* by NaOH treatment), the TiO_2-SiO_2 composite was converted into sodium titanate ($Na_2Ti_3O_7$) with the *in-situ* leaching of the SiO_2.[32] The fiber morphology was well retained but the fibers became highly anisotropic and porous with thorn-like features all-over the fiber backbone. Fig. 5A shows the EDS spectrum of the TiO_2-SiO_2 composites. The peaks for Si, O and Ti were clear from the spectrum. Fig. 5B shows the EDS spectrum of the $Na_2Ti_3O_7$ showing the absence of Si implying the near complete etching of SiO_2 from the TiO_2-SiO_2 composite.

Fig. 6 shows the SEM images of the titanate showing the thorn-like features randomly decorating the fiber backbone. The TEM images of the titanate are shown in Fig. 7. Fig. 7A shows the large area image of the fiber titanate and Fig. 7B-D gives the resolved images of respective fibers. Fig. C and D show the HR-TEM images of the thorn-like features. Fig. 7E shows the layered nature of the $Na_2Ti_3O_7$ and the layer spacing was found to be 0.8 nm; typical for sodium titanate materials.[33,34(a)] The SAED pattern in **Fig. 7F** shows the amorphous nature of the sodium titanate. Fig. 8 A&B shows the powder XRD and Raman spectra of the titanate. The diffraction peak at $2\theta=9.7^0$ ((which is characteristic of the (200) peak of the titanate))[33a,b] and the absence the TiO_2 peaks in the XRD spectrum show that the conversion of TiO_2-SiO_2 composite into the titanate was complete. From the Raman analysis we clearly observe the bands at 295 cm^{-1}, 722 cm^{-1}, and 911 cm^{-1}, respectively, and they confirm the material to be sodium titanate, $Na_2Ti_3O_7$.

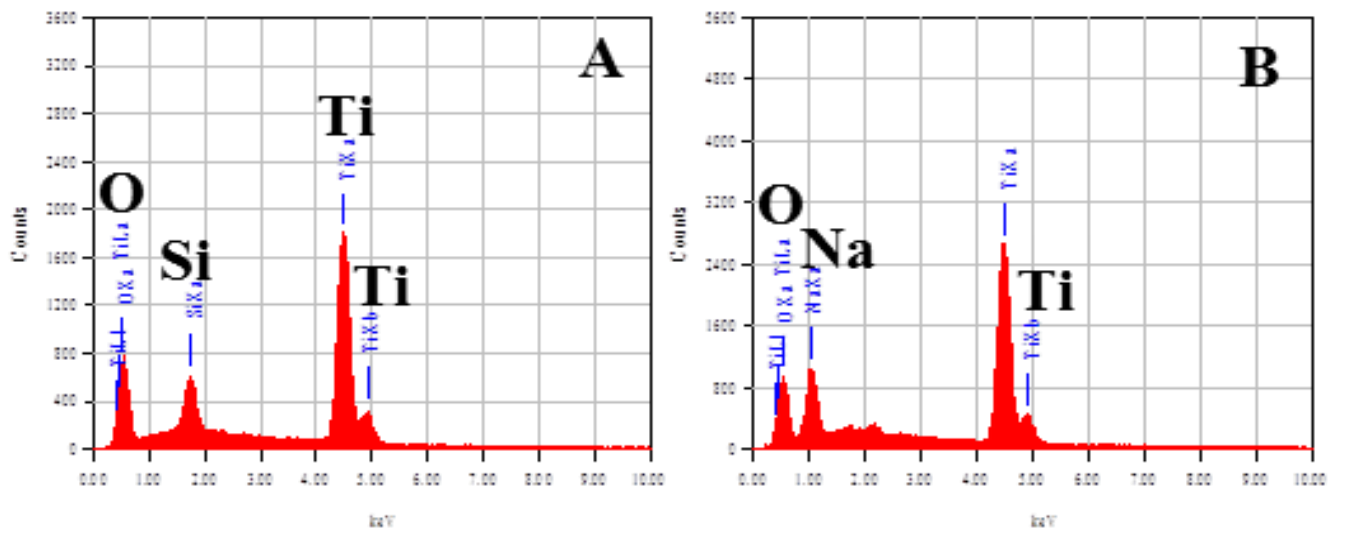

Fig. 5. EDS spectrum of (**5A**) TiO_2-SiO_2 composite and (**5B**) the sodium titanate. A small hump seen around 2 eV (in Fig. B) could be due to the Si impurity (may be from incomplete washing).

Journal Name

RSCPublishing

ARTICLE

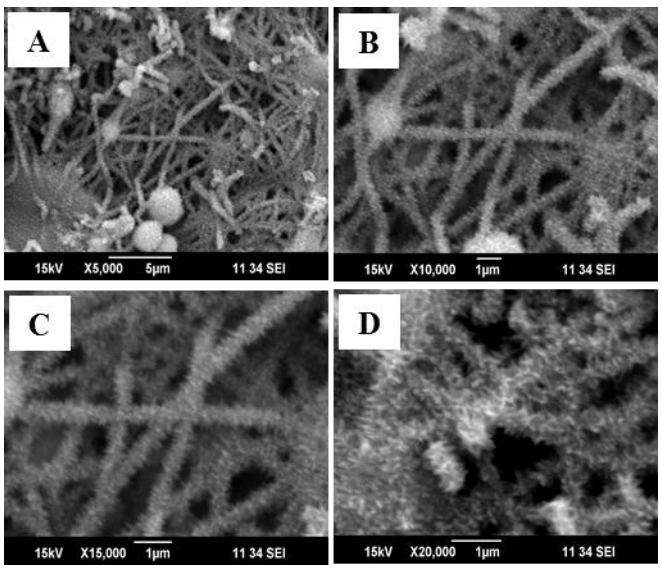

Fig. 6. SEM results of titanates showing thorn like figures originate from the fiber backbone.

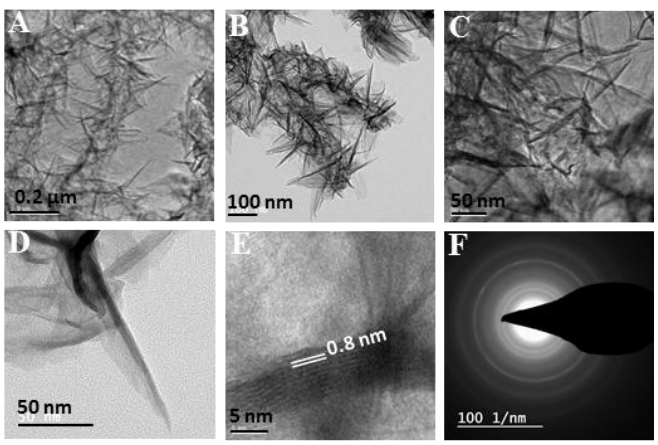

Fig. 7. TEM images of sodium titanates. Fig 7A gives the large area TEM image while resolved images showed by Fig 7B-D. SAED pattern shown by 7F.

The peak 295 cm^{-1} corresponds to the Na–O–Ti bond and peak at 911 cm^{-1} can be attributed to the Ti–O stretching vibration in distorted TiO_6 octahedra.[33c] The Raman band at 722 cm^{-1} represents the Ti–O–Ti stretch vibrational bond in edge-shared TiO_6.[33c] The XPS spectrum of the titanate is given in Fig. 9 (A-D). The wide spectrum of the titanate shown in Fig. 9A implies the absence of the Si peak which further confirms the complete etching of Si during the formation of the titanate. The high-

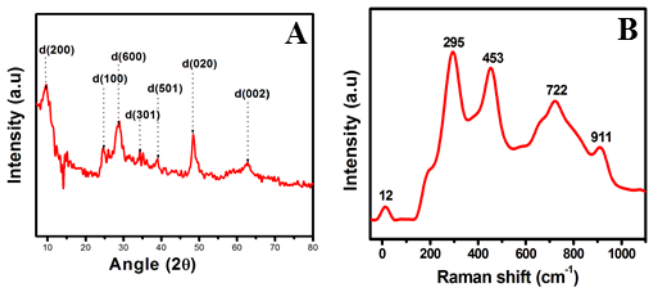

Fig. 8. (A) Powder XRD spectrum and (**B**) Raman spectrum of the $Na_2Ti_3O_7$.

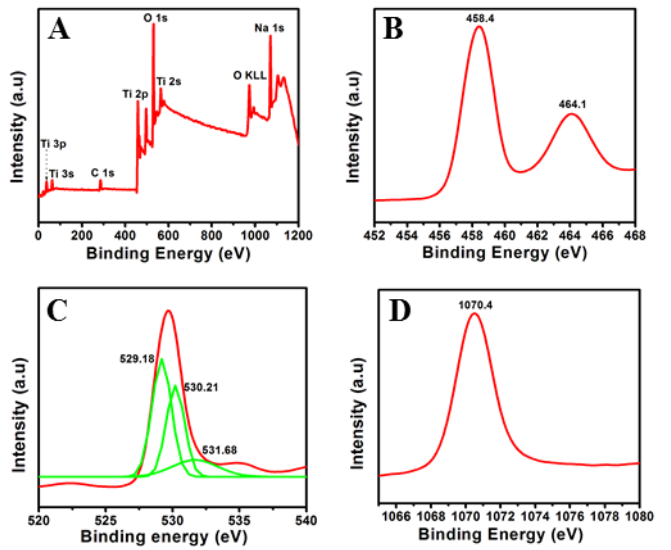

Fig. 9. XPS wide spectrum (**8A**) of $Na_2Ti_3O_7$ showing complete etching of SiO_2 and presence of Na. High-resolution spectrum of Ti (**8B**), O (**8C**) and Na (**8D**).

resolution spectrum of Ti shows the binding energies of Ti 2p3/2 and Ti 2p1/2 centered at 458.4 eV and 464.1 eV, respectively. The O 1s peak (Fig. 9C) showed only a single peak at 530.07 eV corresponding to Ti-O-Ti bonds present in the material.[34] Fig. 9D indicates the presence of Na 1s peak at 1070.4 eV which shows the formation of Ti-O-Na bonds in the $Na_2Ti_3O_7$. The BET surface area of the $Na_2Ti_3O_7$ was measured as 200 m^2/g. A control $Na_2Ti_3O_7$ was also made from electrospun TiO_2 nanofibers (that is without the incorporation of SiO_2) by treatment with NaOH under similar conditions and the resulting $Na_2Ti_3O_7$ showed a BET surface area of 166 m^2/g. This highlights the role of SiO_2 in the chemical transformation process. SiO_2 is an acidic oxide which can be easily etched using NaOH. Thus the TiO_2-SiO_2 composite fibers when treated with NaOH, the chemical transformation of TiO_2 to $Na_2Ti_3O_7$ occurs with the *in-situ* etching of SiO_2. This is the

reason for the high surface area of the $Na_2Ti_3O_7$ obtained from TiO_2-SiO_2 composite fibers than that from TiO_2 fibers.

The $Na_2Ti_3O_7$ upon acid treatment (0.1 N HCl for 12 h) followed by washing (with water and ethanol several times) and

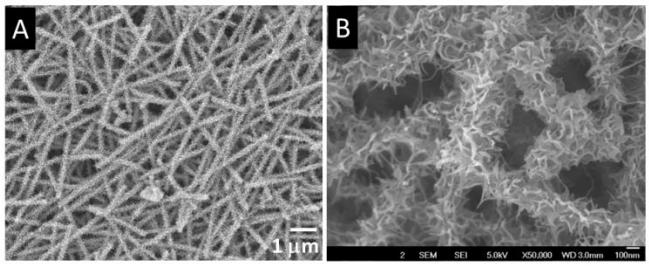

Fig. 10. SEM analysis of TiO_2 in various resolutions further confirms its anisotropic morphology.

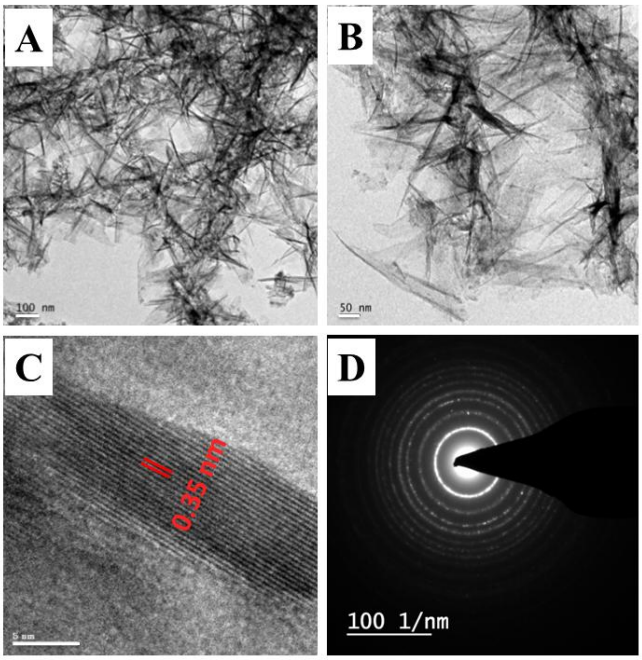

Fig. 11. TEM analysis of TiO_2 nanofibers (**11A** and **11B** gives the large area and resolved TEM images). The lattice spacing (0.35 nm of 101 orientations) had shown by **11C** and **11D** gives the SAED pattern of the same.

low temperature sintering (110 ^{0}C) resulted in the conversion of the $Na_2Ti_3O_7$ into TiO_2 (denoted as the titanate-derived TiO_2 hereafter) with the same morphology as that of the $Na_2Ti_3O_7$, that is fiber architecture with thorn-like features on the fiber backbone. The BET surface area of the TiO_2 (113 m^2/g) was lower than that of the $Na_2Ti_3O_7$ (200 m^2/g) but nearly double than that of the TiO_2-SiO_2 composite (53 m^2/g) and 2.5 times than that of commercial P-25 TiO_2. The average pore sizes and pore volumes of the $Na_2Ti_3O_7$ and the TiO_2 were (5.6 nm and 5.8 nm) and (0.28 cc/g and 0.16 cc/g), respectively. A comparison of the BET isotherms of the P-25 and the titanate-derived TiO_2 is given in Electronic Supplementary Information (ESI) 1.

The TiO_2 fibers were analyzed by microscopy. Fig. 10 and Fig. 11, respectively, show the SEM and TEM images. Low- and high-resolution SEM images (Fig. 10 A&B) show the nearly similar morphology of the $Na_2Ti_3O_7$ for TiO_2 as well, *i.e.* thorn-like features on the fiber architecture resulting in a completely anisotropic morphology. The large area and resolved TEM images (Fig. 11A & 11B) also show the thorn-like morphology of the TiO_2 fibers. Fig. 11C gives the lattice-resolved TEM image of the TiO_2 which confirms its anatase structure with the lattice spacing of 0.35 nm corresponding to the (101) orientation of the anatase TiO_2. The SAED pattern shown by Fig. 11D indicates its polycrystalline nature. The TiO_2 was further characterized by powder XRD and Raman spectra (Fig. 12), respectively. The XRD pattern of TiO_2 further

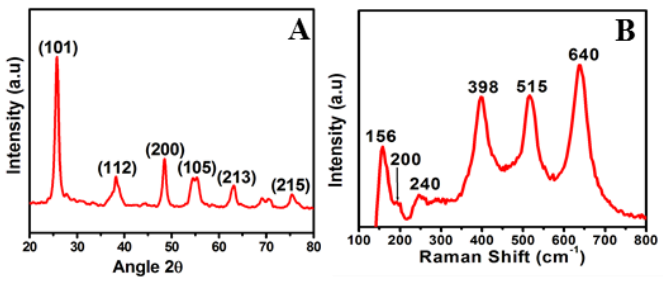

Fig. 12. (A) Powder XRD and (**B**) Raman spectrum of titanate derived TiO_2 nanofibers

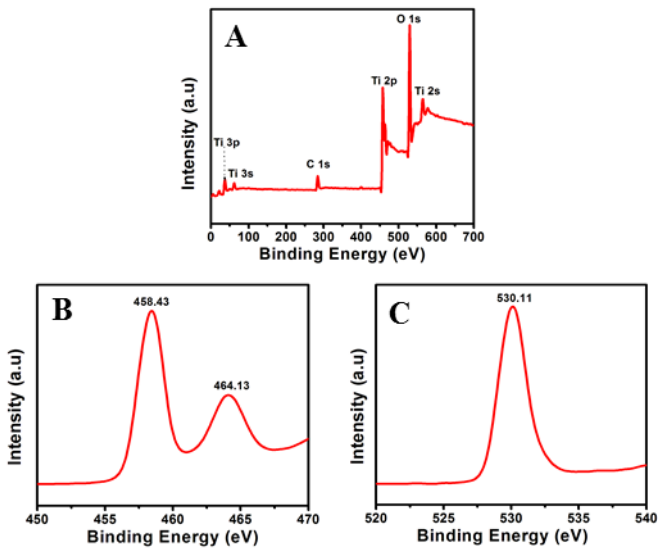

Fig. 13. XPS wide spectrum of TiO_2 (**A**) and the high-resolution spectra of Ti (**B**) and O (**13C**), respectively.

confirms its crystallinity and anatase nature *i.e.* the prominent peak at 2θ=25^0.[35] The peaks are indexed in the spectrum itself and the average particle size of~ 12 nm was calculated from the full-width at half maximum of the major (101) peak by Debye Scherer formula. The major peaks in the Raman spectrum shows that it is anatase TiO_2. According to the factor group analysis from the 15 optical modes ($1A_{1g}+1A_{2u}+2B_{1g}+1B_{2u}+3E_g+2E_u$), six Raman active modes

(A_{1g}, $2B_{1g}$ and $3E_g$) corresponds to anatase phase.[36] The peaks at 640 cm^{-1}, 200 cm^{-1}, 156 cm^{-1} show the three E_g vibrational modes and the peaks 398 cm^{-1}, 515 cm^{-1} represent the B_{g1} and A_{g1} vibrational modes, respectively. XPS analysis was done to confirm the elemental composition and phase purity of TiO_2 (Fig. 13). The binding energies of Ti 2p3/2 and Ti 2p1/2 were centered at 458.43 eV and 464.13 eV, respectively, corresponding to a spin-orbit coupling of 5.7 eV. The single peak for O 1s at 530.11 eV corresponds to Ti-O-Ti bonds in the TiO_2 which further confirms the absence of oxygen related impurities in the TiO_2.

(b) Photovoltaic property of the titanate-derived TiO_2

We fabricated DSCs out of commercial P-25 TiO_2, the TiO_2 nanofibers and the titanate-derived TiO_2 for comparing their photovoltaic performance (Fig. 14A). The photovoltaic parameters of the DSC using P-25 were conversion efficiency (η) of 6.04 % with a current density (J_{sc}) of 10.78 mA cm^{-2}, fill-factor (FF) of 73.55% and an open-circuit voltage (V_{oc}) of 761 mV. The TiO_2 nanofiber (electrospun TiO_2)[25] DSC achieved a η of 5.51 % with a J_{sc} of 10.25 mA cm^{-2}, a FF of 71.27% and a V_{oc} of 753 mV. The DSC using titanate-derived TiO_2 gave a pretty decent performance than the above two. It gave a η of 8.02 % with a J_{sc} of 14.48 mA cm^{-2}, FF of about 73.55% and a V_{oc} of 770 mV. The incident photon-to-current conversion efficiency (IPCE) of the device was ~ 78% whereas the same was ~58% for the P-25-based DSC.

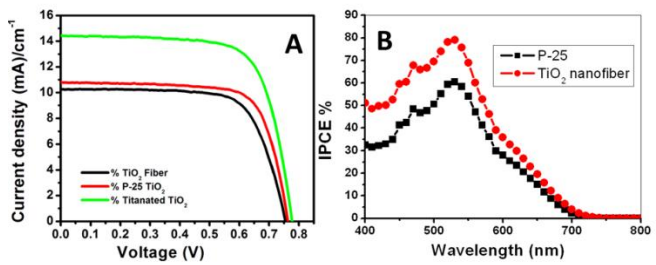

Fig. 14. (**A**) J–V characteristics DSCs of film using titanate-derived TiO_2 and P-25, (**B**) the IPCE (%) of DSCs using titanate-derived TiO_2 and the P-25.

We have analyzed the reasons for the superior performance of the titanate-derived TiO_2 in comparison to the P-25. A comparison of the photovoltaic parameters reveals that high J_{sc} and V_{oc} of the DSC from titanate-derived TiO_2 are the reasons for its high efficiency. The BET surface area of the titanate-derived TiO_2 was measured to be 113 m^2/g which was ~ 2.5 times higher than that of the commercial P-25 (~ 44 m^2/g) (ESI 1). We have quantified the amount of dyes in the DSCs (cells having same thickness and area, respectively) by de-loading them using 0.1 N NaOH. A comparison of the dye-loading data is given in Fig. 15 A which shows enhanced dye adsorption on the titanate-derived TiO_2 than that in the P-25 (owing to the high surface area of the former). Thus high dye loading partly contributed to the increased photocurrent density (J_{sc}). The TiO_2 nanofibers had an average diameter of ~ 250 nm, tens of micron length and have highly roughened surface with thorn-like features projecting out from the fiber backbone. The dimensions and surface features of the fibers were also apt for good light scattering especially at the red part of the solar spectrum. We measured the reflectance of the electrodes from titanate-derived TiO_2 fibers and the P-25 (Fig. 15 B). It can be seen that the titanate TiO_2 fibers scattered more photons at the red part of the spectrum than the P-25 implying more photon confinement within the TiO_2 fiber electrode. This also might have contributed to the increased J_{sc} value.

Electrochemical impedance spectra (EIS) of the DSCs were measured under dark condition under an applied forward bias of 0.7 V to find the recombination resistance values. EIS result is depicted in the Nyquist plot (Fig. 15 C). The Nyquist plot for an ideal DSC device will show three semicircles corresponding to charge transfer at the counter electrode-electrolyte interface (appears in high frequency range), charge transfer at the oxide-electrolyte interface (R_{ct}) (appears in medium frequency range) and ion diffusion through the electrolyte (appears in lower frequency range). The recombination resistance (middle frequency) is more for the titanate-derived TiO_2 (larger semicircle) than for the P-25 (smaller semicircle) implying reduced electron recombination for the former. This is further evident from the lifetime of the electrons in the respective DSCs measured from the Bode phase plots (Fig. 15 D). The lifetime of the electrons is related to the peak of the Bode phase plot by the relation: $T_s = 1/2\pi f_{peak}$, where f_{peak} corresponds to the frequency maximum. The respective electron lifetimes were calculated to be 13 ms and 16 ms for P-25 and the titanate-derived TiO_2. Increased lifetime of electrons in the fiber DSC implies reduced electron recombination which is reflected in the increased V_{oc} and J_{sc} of the DSC made from the titanate derived TiO_2. While reduced recombination is one of the reasons for the observed high V_{oc}, yet another reason can be the chemical composition of the TiO_2. The titanate TiO_2 nanofiber

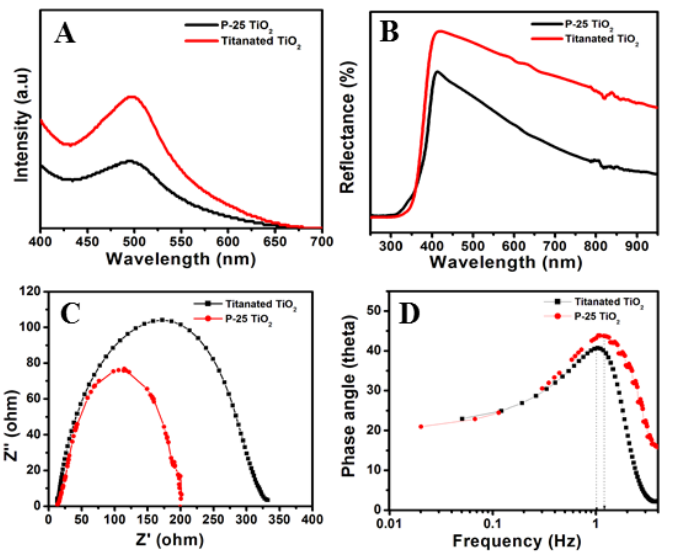

Fig. 15. A comparison of the dye-loading (A), reflectance (B) data on the two electrodes. And the(C) Nyquist plot and (D) Bode phase plot of two DSCs at dark also figured.

is phase pure (anatase), the P-25 is a mixture of ~ 75% anatase (band-gap of 3.2 eV) and ~ 25% rutile (band-gap of 3.0 eV). Thus the apparent Fermi level of P-25 will be slightly lower than that of the titanate TiO_2 and hence the observed variations in the V_{oc}. Thus it can be summarized that the high J_{sc} and V_{oc} are the primary reasons for the enhanced performance of the titanate-derived TiO_2 in comparison to the P-25 TiO_2.

Conclusions

TiO_2 nanofibers resembling the morphology of yellow bristle grass were fabricated from TiO_2-SiO_2 composite nanofibers by a soft chemical transformation and etching process. The soft etching process also involved chemically transforming the TiO_2 with the *in-situ* etching of SiO_2 by concentrated NaOH under room temperature and ambient pressure. The initial TiO_2-SiO_2 composite fibers, the chemically transformed $Na_2Ti_3O_7$ fibers and the titanate-derived TiO_2 fibers with the morphology of yellow bristle grass were characterized by spectroscopy and microscopy. A comparison of the dye-sensitized solar cell performance of the commercially available P-25, the TiO_2 nanofibers and the present TiO_2 with the yellow bristle grass morphology showed a superior performance for the final one (an efficiency of 8.02 % vs. that for the commercial P-25 TiO_2, 6.039 %). We anticipate many promising applications for the titanate-derived TiO_2 in anti-reflecting coatings, Li-ion battery, environmental remediation, etc.

Acknowledgements

The authors acknowledge financial support from Ministry of New and Renewable Energy (MNRE) and Solar Energy Research Initiative (SERI), Dept. of Science and Technology (DST), respectively, of Govt. of India.

Notes and references

[a] Amrita Centre for Nanosciences and Molecular Medicine, Amrita Institute of Medical Sciences, Amrita Vishwa Vidyapeetham, AIMS PO, Kochi 682041, Kerala, India. Email: sreekumarannair@aims.amrita.edu.

† Electronic Supplementary Information (ESI) available [a comparison of the BET surface area of P-25 TiO_2 and titanate-derived TiO_2]. See DOI: 10.1039/b000000x.

1. (a) B. O'Regan and M. Gr¨atzel, *Nature*, 1991, **353**, 737 (b) M. Gr¨atzel, *Nature*, 2001, **414**, 338
2. (a) H. J. Snaith, *J. Phys. Chem. Lett.*, 2013, **4**, 3623–3630. (b)
3. (a) L. Etgar, P. Gao, Z. Xue, Q. Peng, A. K. Chandiran, B. Liu, Md. K. Nazeeruddin, and M. Grätzel, *J. Am. Chem. Soc.*, 2012, **134**, 17396–17399. (b) J. Burschka, N. Pellet, S.-J. Moon, R. Humphry-Baker, P. Gao, M. K. Nazeeruddin, and M. Gratzel, *Nature*, 2013, **499**, 316.
4. (a)T. Kasuga, M. Hiramatsu, A. Hoson, T. Sekino, K. Niihara, *Langmuir*, 1998, **14**, 3160. (b)T. Kasuga, M. Hiramatsu, A. Hoson, T. Sekino and K. Niihara, *Adv. Mater.*, 1999, **11**, 1307.
5 A. S. Nair, Z. Peining, V. J. Babu, Y. Shengyuan and S. Ramakrishna, *Phys. Chem. Chem. Phys.*, 2011, **13**, 21248-21261.
6. S. H. Lim, J. Luo, Z. Zhong, W. Ji and J. Lin, *Inorg. Chem.*, 2005, **44**, 4124.
7. J. Sundaramurthy, V. Aravindan, P. S. Kumar, S. Madhavi and S. Ramakrishna, *J. Phys. Chem. C*, 2014, DOI: 10.1021/jp412787z.
8. (a) X. Chen and S. S. Mao, *Chem. Rev.*, 2007, **107**, 2891-2959. (b) G. Wang, L. Zhang and J. Zhang, *Chem. Soc. Rev.*, 2012, **41**, 797-828. (b) V. Etacheri, R. Marom, R. Elazari, G. Salitra and D. Aurbach, *Energy Environ. Sci.*, 2011, **4**, 3243-3262.
9. A. Fujishima, and K. Honda, *Nature*, 1972, **238**, 37.
10. Fox, M. A.; Dulay, M. T. *Chem. Rev*. 1993, **93**, 341.
11. M. Inagaki, Y. Nakazawa, M. Hirano, Y. Kobayashi, and M. Toyoda, *Int. J. Inorg. Mater*., 2001, **3**, 809.
12. M. Schraml-Marth, A. Wokaun, and A. B. Fresenius, *J. Anal. Chem*., 1991, **341**, 87-91
13. D. J. Yang, Z. F. Zheng, H. Y. Zhu, H. W. Liu and X. P. Gao, *Adv. Mater.*, 2008, **20**, 2777.
14. M. M. Khin, A. S. Nair, V. J. Babu, R. Murugan and S. Ramakrishna, Energy Environ. Sci., 2012, **5**, 8075-8109
15. M. R. Hoffmann, S. T. Martin, W. Choi, D. W. Bahnemann, *Chem. Rev.*, 1995, **95**, 69–96.
16. K. Hashimoto, H. Irie and A. Fujishima, *Jpn. J. Appl. Phys.*, 2005, **44**, 8269.
17. (a) V. A. Ganesh, H. K. Raut, A. S. Nair and S. Ramakrishna, *J. Mater. Chem*., 2011, **21**, 16304–16322. (b) P. Ragesh, V. A. Ganesh, S. V. Nair and A. S. Nair, *J. Mater. Chem. A*, 2014, 2, 14773-14797. (c) V. A. Ganesh, S. S. Dinachali, A. S. Nair, and S. Ramakrishna, *ACS Appl. Mater. Interfaces*, 2013, **5**, 1527–1532. (d) P. Ragesh, S. V. Nair and A. S. Nair, RSC Adv., 2014, 4, 38498-38504.
18. G. K. Mor, K. Shankar, M. Paulose, O. K. Varghese, and C. A. Grimes, *Nano Lett.*, 2006, 6, 215–218.
19. J. R. Jennings, A. Ghicov, L. M. Peter, P. Schmuki, and A. B. Walker, *J. Am. Chem. Soc.*, 2008, **130**, 13364–13372.
20. Sara Thomas, T. G. Deepak, G. S. Anjusree, T. A. Arun, Shantikumar V. Nair and A. Sreekumaran Nair, *J. Mater. Chem. A*, 2014, **2**, 4474–4490.
21. M. Y. Song, D. K. Kim, K. J. Ihn, S. M. Jo, and D. Y. Kim, Nanotechnology, 2004, **15**, 1861.
22. B. H. Lee, M. Y. Song, S.-Y. Jang, S. M. Jo, S.-Y. Kwak, and D. Y. Kim, *J. Phys. Chem. C*, 2009, **113,** 21453–21457.
23. T. A. Arun, A. A. Madhavan, D. K. Chacko, G. S. Anjusree, T. G. Deepak, S. Thomas, S. V. Nair and A. S. Nair, *Dalton Trans.*, 2014, **43**, 4830-4837.
24. (a) A. S. Nair, Z. Peining, V. J. Babu, Y. Shengyuan, P. Shengjie and S. Ramakrishna, *RSC Adv.*, 2012, **2**, 992-998. (b) D. K. Chacko, A. A. Madhavan, T. A. Arun, S. Thomas, G. S. Anjusree, T. G. Deepak, A. Balakrishnan, K. R. V. Subramanian, N. Sivakumar, S. V. Nair and A. S. Nair, *RSC Adv.*, 2013, **3**, 24858-24862.
25. A. S. Nair, R. Jose, Y. Shengyuan and S. Ramakrishna, *J. Colloid Interface Sci.*, 2011, 353, 39-45.
25. T. G. Deepak, G. S. Anjusree, K. R. Narendra Pai, D. Subash, S. V. Nair and A. S. Nair, *RSC Adv.*, 2014, **4**, 27084-27090.
26. (a) T. A. Arun, D. K. Chacko, A. A. Madhavan, T. G. Deepak, G. S. Anjusree, T. Sara, S. Ramakrishna, S. V. Nair and A. S. Nair, *RSC Adv.*, 2014, **4**, 1421-1424. (b) T. G. Deepak, D. Subash, G. S.

Anjusree, K. R. Narendra Pai, S. V. Nair , and A. S. Nair, *ACS Sustainable Chem. Eng.*, 2014, **2**, 2772–2780.

27. A. S. Nair, Z. Peining, V. J. Babu, Y. Shengyuan, P. Shengjie and S. Ramakrishna, *RSC Adv*., 2012, **2**, 992-998.
28. (a) M.Bahtat,J.Munier,C.Bovier,H.Roux and J.Serughetti, *Journal of Non-Crystalline Solids*, 1992, **147&148**, 123-126. (b) I. R. Beattie and T. R. Gilson, *Proc. R. Soc. Lond. A*., 1968 **307**, 407-429
30. A. S. Nair, P. Zhu, V. J. Babu, S. Yang, T. Krishnamoorthy, R. Murugan, S. Peng and S. Ramakrishna, *Langmuir*, 2012, **28**, 6202.
31. A. S. Nair, Z. Peining, V. J. Babu, Y. Shengyuan, Y. Shengjie and S. Ramakrishna, *RSC Adv*., 2012, **2**, 992-998.
32. (a) C.-C. Tsai and H. Teng, *Chem. Mater*., 2006, **18**, 367. (b) E. Morgado Jr, M. A. S. de Abreu, G. T. Moure, B. A. Marinkovic, P. M. Jardim and A. S. Araujo, *Chem. Mater*., 2007, **19**, 665.
33. (a) J. Yang, Z. Jin, X. Wang, W. Li, J. Zhang, S. Zhang, X. Guo and Z. Zhang, *Dalton Trans*., 2003, 3898. (b) D. V. Bavykin, J. M. Friedrich and F. C. Walsh, *Adv. Mater.*, 2006, **18**, 2807. (c) H.Liu, D.Yang, Z. Zheng, Xuebin Ke, Eric Waclawik, H. Zhu and Ray L. Frost, *J. Raman Spectrosc*., 2010, **41**, 1331–1337
34. A. S. Nair, Z. Peining, V. J. Babu, Y. Shengyuan, Y. Shengjie and S. Ramakrishna, *RSC Adv*., 2012, **2**, 992
35. Q. Wang, S. Ito, M. Gratzel, F. Fabregat-Santiago, I. M. Sero, J. Bisquert, T. Bessho and H. Imai, *J. Phys. Chem. B*, 2006, **110**, 25210–25221
36. (a)T. Ohsaka, F. Izumi and Y. Fujiki, *J. Raman Spectrosc.*, 1978, **7**, 321–324. (b) M.Ocana, J.V. Garcia-Ramos," and Carlos J. Serna", *J. Am Ceram Soc*., 1992, **75**, 7, 2010-12.